



HAL
open science

Tunable morphologies of ultrathin ZnO nanostructures synthesized by a plasma afterglow-assisted oxidation process and their photocatalytic properties

T. Pérez, A. Imam, D. Pilloud, J. Ghanbaja, P. Miska, T. Belmonte, T. Gries

► To cite this version:

T. Pérez, A. Imam, D. Pilloud, J. Ghanbaja, P. Miska, et al.. Tunable morphologies of ultrathin ZnO nanostructures synthesized by a plasma afterglow-assisted oxidation process and their photocatalytic properties. *Plasma Sources Science and Technology*, 2019, 28 (4), pp.045008. 10.1088/1361-6595/ab1238 . hal-02144871

HAL Id: hal-02144871

<https://hal.univ-lorraine.fr/hal-02144871v1>

Submitted on 21 Nov 2020

HAL is a multi-disciplinary open access archive for the deposit and dissemination of scientific research documents, whether they are published or not. The documents may come from teaching and research institutions in France or abroad, or from public or private research centers.

L'archive ouverte pluridisciplinaire **HAL**, est destinée au dépôt et à la diffusion de documents scientifiques de niveau recherche, publiés ou non, émanant des établissements d'enseignement et de recherche français ou étrangers, des laboratoires publics ou privés.

Tunable morphologies of ultrathin ZnO nanostructures synthesized by a plasma afterglow-assisted oxidation process and their photocatalytic properties

T Perez¹, A Imam¹, D Pilloud¹, J Ghanbaja¹, P Miska¹, T Belmonte² and T Gries²

¹ Université de Lorraine, Institut Jean Lamour, UMR CNRS 7198, NANCY, F-54011, France

² CNRS, Institut Jean Lamour, UMR CNRS 7198, NANCY, F-54011, France

Keywords

Microwave plasma afterglow, ultrathin ZnO nanostructures, photocatalysis

Abstract

The fast growth of ultrathin zinc oxide nanostructures is reported in this study, by using a flowing microwave plasma oxidation method: zinc films coated by a thin copper buffer layer are oxidized in low-pressure afterglow. This work highlights the versatility of plasma afterglow treatments and demonstrates that the morphology of ZnO nanostructures (nanowires, nanoribbons and nanocombs) can easily be controlled with good reproducibility by adjusting experimental parameters such as the working pressure during the oxidation process. The rapid growth of ultrathin nanostructures (~1 min) is due to the afterglow area which is a very oxidizing medium since it contains high concentrations of oxygen atoms and excited oxygen molecules. The surface morphology and structural and optical properties of the as-synthesized nanostructures are studied by means of SEM, HRTEM and UV–visible absorption, respectively. Ultrathin ZnO nanowires and nanoribbons with high aspect ratios exhibit excellent photocatalytic activity for the degradation of a model organic dye: methyl orange (MO), by comparison with pure ZnO thin films without nanostructures and thick ZnO nanowires synthesized by thermal oxidation. These results are supported by photocurrent measurements. The enhancement in photocatalytic performance could be attributed to higher surface area and higher transfer efficiency of photoinduced charge carriers to the surface of ultrathin nanowires and nanoribbons. The reusability of ZnO nanowire samples is also investigated by recording the photoactivity after several cycles of photodegradation.

1. Introduction

The use of metallic oxide semiconductors as photocatalysts has been widely studied due to its potential applications in the removal of hazardous pollutants and in energy fuel production such as water splitting [1, 2]. Among the various semiconductors, ZnO has emerged as one of the most promising and most widely investigated photocatalysts with TiO₂ due to its excellent oxidation ability, its physical, chemical and thermal stability, its non-toxicity, its abundance in nature and its low cost. Photocatalysis is a promising technique for the degradation of inorganic and organic pollutants in air and water. Especially, ZnO seems to be an ideal photocatalyst for practical applications on the wastewater treatments. For more details, the reviews of Kumar and Rao [3] and Lee et al [4] give an overview on recent developments of zinc oxide-based photocatalysts in water treatment technology.

The photodegradation efficiency can be improved through a better design of the ZnO structure. The surface area and thus the morphology are factors of paramount importance which affect directly the photocatalytic efficiency of metallic oxide semiconductors [5–8]. As a consequence, ZnO nanopowders with different morphologies have been extensively studied as photocatalysts in suspension, which can provide high enhancement of photocatalytic activity [9, 10]. However, the use of ZnO nanostructures with high aspect ratio (nanowires, nanoribbons, etc.) grown on substrates offers as main advantage to overcome the difficult and expensive process for the separation and recycling of ZnO powders [11]. Furthermore, these nanostructures offer a larger surface-to-volume ratio by comparison with nanoparticles deposited on a flat substrate and hence are expected to show a higher photocatalytic activity [12]. The challenge in the widespread use of ZnO as photocatalyst is to limit the recombination of photogenerated charge carriers, which is typically faster than the production rate of reactive oxidation species. This recombination step lowers the quantum yield and causes energy wasting. Thereby, different strategies are employed to promote charge separation such as doping with metallic and non-metallic elements, coupling with semiconductors or modifying with noble metals. Improved segregation efficiency for photogenerated electron and hole pairs can also be obtained with ultrathin ZnO nano-objects: since the mean free path of charge carriers is also in nanometric scale, the photogenerated electrons and holes can reach the surface of the nanostructured material and are readily available for degradation

reactions [13, 14]. This leads to a reduction of electron–hole recombination possibilities and thus to an enhancement of the photocatalytic activity.

Only few studies have been reported on the synthesis of ultrathin one dimensional ZnO nanostructures with most of them achieved using chemical solutions [15–17]. ZnO nanostructures can also be synthesized through the thermal oxidation of Zn foils [18, 19]. However, this simple and cost-effective approach leads to nanowires with large diameters (typically between 20 and 200 nm) and requires relatively long treatment durations (~2 h). In this work, we propose another strategy to synthesize ultrathin ZnO nanostructures with high growth rates, by using flowing microwave plasma afterglow-assisted oxidation treatments. Plasma afterglow-assisted oxidation processes enable the synthesis of a large variety of metallic oxide nanostructures, even at atmospheric pressure [20–22]. Indeed, afterglow processes benefit from a higher reactivity of the oxidizing gas phase at moderate temperature compared to thermal heating processes, because of the presence of active oxygen species like oxygen atoms or metastable states of O₂. In previous work [23], the growth of ultrathin nanowires with high aspect ratios was reported for optimal experimental conditions (treatment duration, furnace temperature, oxygen concentration, etc). In the present study, different morphologies of nanostructures (nanowires, nanoribbons or nanocombs) are synthesized by this process and these morphologies can be easily controlled with good reproducibility by adjusting experimental conditions, especially the total pressure in the reactor. Furthermore, the photocatalytic activity of these nanostructures is systematically investigated by measuring the degradation of a commonly-used organic dye in aqueous solution: methyl orange (MO). The photocatalytic activity of these ultrathin ZnO nanostructures will be also compared with the properties of flat ZnO thin films and thick ZnO nanowires.

2. Experimental procedure

2.1. Synthesis of ZnO nanostructures

ZnO nanostructures are synthesized by oxidation of Cu/Zn stacks (50 nm Cu/950 nm Zn) formerly deposited by DC magnetron sputtering (80W) on soda lime glass (SLG) substrates and on fluorine-doped tin oxide coated glass slide (FTO, 7 Ω sq⁻¹). The experimental procedure was

described in detail elsewhere [23]. Thicknesses are set by adjusting the sputtering time. The distance between the sample and the targets (50 mm in diameter, 3 mm thick and >99.99% purity for Zn target and >99.95% purity for Cu target) is 100 mm. The base pressure in the sputtering chamber is 5×10^{-4} Pa and thin films are deposited at a pressure of 0.6 Pa in a 10 vol% H₂–90 vol% Ar mixture. These films are oxidized by using a flowing microwave afterglow at low pressure (figure 1). A surface wave-driven plasma is ignited in a fused silica tube (inner diameter = 5 mm) by exposure to 2.45 GHz microwaves launched with a Surfatron. The microwave power absorbed by the plasma is kept constant at 200 W. An Ar-2 vol% O₂ mixture, flowing at 560 standard cubic centimetres per minute (sccm), is used as plasma gas. The samples are located in a quartz reactor tube (internal diameter of 28 mm) downstream the plasma glow region, at a distance of 60 cm from the plasma gap. The treatment starts when the plasma is turned on ($t = 0$) concurrently with the injection of the reactive gas. The temperature of the sample during oxidation is controlled by an additional furnace (set at 500 °C).

2.2. Plasma and thin film characterizations

The surface morphology is imaged with a high-resolution scanning electron microscope (SEM) Philips XL-FEG 30 equipped with a TLD detector (through the lens detector). The morphology, size distribution, composition and crystallographic features of the as-synthesized nanostructures are characterized by high-resolution TEM (HRTEM). Nanostructures are taken off from the samples by scratching the surface upon a holey carbon nickel grid. HRTEM investigations are carried out using a JEM—ARM 200F Cold FEG TEM/STEM operating at 200 kV and equipped with a spherical aberration (Cs) probe and image correctors (point resolution 0.12 nm in TEM mode). Transmittance measurements are done with a Cary 5000 UV–vis-NIR spectrophotometer in the ultraviolet, visible and near-infrared ranges. Electron density measurements are carried out by using a 26.5 GHz microwave interferometer (Miwitron MWI 2650). This technique based on the determination of the refractive index of the plasma permits measurements of electron density at moderate pressure [24, 25]. For optical emission spectroscopy (OES) measurements, the afterglow light is collected by an optical fibre connected to a 550 nm focal length monochromator (Jobin-Yvon TRIAX 550) equipped with a 1800 grooves mm⁻¹ grating. The spectrometer is coupled with a Horiba Jobin-Yvon i-Spectrum Two iCCD detector.

2.3. Photocatalytic measurements

The photocatalytic activity of as-prepared samples (2 cm² × 1 cm) is evaluated by the degradation of MO dye (200 ml, 20 mg l⁻¹) under light irradiation from a Xenon lamp (Newport Xe 300 W ozone free) with an air mass filter (AM 1.5 G) to better match the total solar spectrum. Before illumination, the reactor is magnetically stirred in the dark for 30 min to reach the adsorption–desorption equilibrium between the photocatalyst and the dye. The irradiance reaching the photoactive surface is measured with a PM100D Thorlabs radiometer equipped with a 200–1100 nm sensor and is set equal to 100 mW cm⁻². The concentration of MO is monitored by recording variations in the characteristic absorption band (464 nm) using an Ocean Optics S2000 spectrometer.

Photoelectrochemical measurements of as-prepared samples are performed by a SP150 BioLogic potentiostat connected to a standard three electrode cell: Pt wire as the counter electrode, a saturated Ag/AgCl electrode as reference electrode and FTO glass coated with nanostructured ZnO films (1 cm × 1 cm) as the working electrode. 0.1M Na₂SO₄ aqueous solution is used as electrolyte. The photocurrent response is recorded at a constant potential of +0.30 V versus the reference electrode.

3. Results and discussion

3.1. Plasma diagnostics

Figure 2(a) is a plot of the electron density estimated by interferometry as a function of distance from the Surfatron launcher exit (in the small-diameter quartz tube). The spatial distribution of electron density was assumed to be constant, radially. Therefore, this assumption gives the average value of the density across the line-of-sight path of the millimetre wave. The detection limit of microwave interferometer in the present configuration is approximately 1.0×10^{11} cm⁻³. As generally observed in Surface Wave Discharges (SWD), the electron density decreases linearly with the distance in the plasma column up to a critical density for surface wave propagation ($n_e \sim 3 \times 10^{11}$ cm⁻³) [26]. This position corresponds to the transition from plasma to the early afterglow (at about 10.5 cm from Surfatron in our conditions).

The light emitted from the afterglow is weak and only visible in the dark with the naked eye. Three main contributions of oxygen are observed by OES: OH($A^2\Sigma^+$, $v' = 0 \rightarrow X^2\Pi$, $v'' = 0$) at 306 nm, the green line of atomic oxygen O($^1S \rightarrow ^1D$) at 557.7 nm and the atmospheric band of O₂($b^1\Sigma_g^+ \rightarrow X^3\Sigma_g^-$) at 762 nm (figure 2(b)). An argon line appears at 763.5 nm that is removed to determine the rotational temperature of the gas according to data available in [27]. The rotational temperature of O₂(b) state is generally considered as a good approximation of the kinetic temperature of O₂ molecules in the ground state. A temperature of 330 ± 30 K is obtained, confirming the relatively low temperature of the afterglow. In a previous work, the absolute density of oxygen atoms was determined by NO titration method using an Ar-1.4 vol% NO gas mixture [28]. This technique was performed at the end of the small fused silica tube, as a function of the total pressure. This two-step method, described in [29], leads, for example, to an oxygen atom concentration $[O] = 1.1 \pm 0.3 \times 10^{15} \text{ cm}^{-3}$ at a pressure of 200 Pa. These results are consistent with the calculated values predicted by Kutasi *et al.* by using self-consistent theoretical models developed to investigate the early and remote flowing afterglows of a surface-wave Ar-O₂ microwave discharge generated in a reactor with geometry close to that of this study [30, 31].

3.2. Morphology and crystallographic structure of ZnO nanostructures

Figure 3 depicts SEM micrographs of nanostructures grown for 1 min of flowing afterglow oxidation as a function of the working pressure. By contrast with thermal oxidation process which requires relatively long treatment duration to obtain nanowires, the rapid growth of nanostructures in this study is attributed to the non-equilibrium behaviour of the afterglow, which provides directly active species on the sample surface. In these experimental conditions, the afterglow contains a concentration of oxygen atoms of about 10^{15} cm^{-3} and a high concentration of excited oxygen molecules like O₂($a^1\Delta_g$), O₂($X^3\Sigma_g^-$) and to a lesser extent, O₂($b^1\Sigma_g^+$) [30]. As described in a previous work [23], copper thin film plays also a key role in the growth mechanism: this buffer layer prevents film evaporation and allows treatments at temperatures that are higher than the melting temperature of zinc (m. p. = 419.5 °C) mainly due to the formation of CuZn₅ intermetallic by interdiffusion, which melts at a higher temperature. The growth mechanism of ZnO nanowires seems to be driven by diffusion at grain boundaries, Zn having higher oxygen affinity than Cu. As generally observed in thermal oxidation at moderate temperature, zinc oxidation involves Zn ions outward diffusion from

Zn-ZnO interface to the surface through grain boundaries or defects, creating sites on surface from which ZnO nanowires grow [19]. The surface morphology is clearly highly dependent on the pressure. Ultrathin nanowires with fairly high surface density are synthesized at 200 Pa. The average length of nanowires is estimated to be 750 nm with a mean diameter of 6 nm [23]. The growth of nanoribbons is observed at 1000 Pa. Nanoribbons are longer (average length ~ 1500 nm) with a mean width of approximately 60 nm and an assessed thickness of about 5 nm (confirmed by TEM measurements). As the total pressure is increased to 2000 Pa during afterglow oxidation treatment, a large number of long ZnO nanocombs are observed among nanoribbons. ZnO nanocombs with dense nanowire branches grown on one side of nanoribbons contain very thin, straight, aligned and evenly spaced branches (~ 20 wires μm^{-1}). The evolution of morphology with the working pressure could be mainly attributed to density profiles of active species which depend on experimental conditions including pressure, as observed by Kutasi et al. They especially observed a large increase in the main active oxygen species densities ($\text{O}(^3\text{P})$, $\text{O}_2(a)$ and $\text{O}_2(b)$) with pressure in the late afterglow (see figure 8 in [30]), whereas their lifetimes are relatively independent of the value of pressure. Therefore, higher active oxygen species densities seem to promote the growth of nanoribbons and nanocombs.

Nanoribbons exhibit high aspect ratios with a non-uniform width distribution within a nanoribbon (figures 4(a) and (b)). Figures 4(c) and (d) show HRTEM micrographs taken from an individual nanoribbon, including its fast Fourier transform pattern. As in the case of nanowires [23], the values of measured angles and distances between atomic planes reveal that all the tested nanoribbons can be indexed by the ZnO wurtzite structure (space group: $\text{P6}_3\text{mc}(186)$, hexagonal, $a = b = 3.2494 \text{ \AA}$, $c = 5.2038 \text{ \AA}$) [32]. Again, ZnO nanoribbons have also high-quality, single-crystalline structure with no preferential growth direction after analysis of a large set of nanoribbons randomly taken in different areas on the surface of the sample. Copper is present in nanostructures only as traces, with concentrations typically inferior to 1 at% (EDS analyses). In both cases, the growth mechanism is based on the outward diffusion of zinc ions through grain boundaries and defects in overlayers underneath nanostructures [23].

3.3. Photocatalytic activity of ZnO nanostructures

Methyl orange (MO) is selected as a model organic pollutant to evaluate the photocatalytic activity performance of ZnO nanostructures with different morphologies. Figure 5(a) shows

the UV–visible absorption spectra of MO solution at different irradiating intervals with ultrathin ZnO nanowires as photocatalyst. The absorption peak of MO at 464 nm decreases with the exposure duration, indicating that the concentration of MO in the solution is reduced gradually. This evolution is consistent with the corresponding pictures of the MO solution, figure 5(b). Figure 5(c) shows the relative concentration (C/C_0) of MO as a function of time under light irradiation, where C is the concentration of MO at irradiation time (t) and C_0 is the concentration of the dye before sample immersion. As a control, the absorbance peak of MO solution is also monitored with photocatalysts in the dark and without photocatalysts under light illumination. In the latter case, MO solution is irradiated to estimate the degree of degradation of MO only by photolysis and ensure the action of photocatalytic reaction on MO by all the catalysts. It can be observed that the MO dye concentration after magnetic stirring in the dark for 30 min only slightly decreases in presence of ZnO, indicating that the adsorption of MO on the surface is limited after the adsorption–desorption equilibrium is reached.

In order to evaluate the influence of ultrathin nanostructures on MO degradation, the photocatalytic activities of ZnO nanowires and ZnO nanoribbons are compared with pure ZnO thin films without nanostructures and ZnO nanowires with larger diameters (mean diameter of about 60 nm). Pure ZnO thin films and thick nanowires have been synthesized by thermal oxidation for 3 h in air at 300 °C and 400 °C respectively, from 1 μm thick Zn thin films formerly deposited by DC magnetron sputtering [33]. The results indicate that ultrathin ZnO nanowires and nanoribbons exhibit similar trends with a good photocatalytic activity in aiding the degradation of MO, approximately 92% after irradiation for 420 min. By comparison, the photolysis process, pure ZnO without nanostructures and thick ZnO nanowires (mean diameter of about 60 nm) under identical conditions present degradation of MO of 18%, 33% and 62%, respectively. The photodegradation kinetics of MO could be fitted to a pseudofirst order reaction and the rate equation is expressed as: $\ln(C/C_0) = -kt$. The apparent reaction rate constant k is calculated to be $1.5 \times 10^{-3} \text{ min}^{-1}$ ($R^2 = 0.9830$) $2.5 \times 10^{-3} \text{ min}^{-1}$ ($R^2 = 0.9837$), $7.0 \times 10^{-3} \text{ min}^{-1}$ ($R^2 = 0.9961$) and $6.5 \times 10^{-3} \text{ min}^{-1}$ ($R^2 = 0.9957$) for pure ZnO thin film without nanostructures, thick ZnO nanowires ($\varnothing \sim 60 \text{ nm}$) synthesized by thermal oxidation, ultrathin ZnO nanowires ($\varnothing \sim 6 \text{ nm}$) and ZnO nanoribbons synthesized by plasma afterglow oxidation process, respectively. The corresponding squares of linear correlation coefficients (R^2) confirm a pseudo-first order reaction in degradation kinetics.

These rate constant values confirm that the degradation rate constant is higher for ZnO catalysts with ultrathin nanostructures. The surface area plays a significant role on the photocatalytic activity. Thus, nanostructured materials offer generally enhanced photodegradation kinetics due to their extremely large surface to volume ratios. Moreover, the photocatalytic activity depends also on the effectiveness of photogenerated charge carrier separation: photoinduced electrons and holes have strong oxidation and reduction activities leading to MO degradation. The main limitation is due to the high recombination rate of these charge carriers. In this work, ultrathin nanowires and nanoribbons provide at least one dimension extremely low (<10 nm). In this case, charge carriers need to diffuse only over a short distance to reach active sites on the surface and react with water molecules before recombination. High crystallinity can also enhance the charge diffusion and thus decrease the possibility of charge recombination within nanostructures. On the other hand, the presence of a small amount of copper in the sublayer (*i.e.* underneath the nanostructures) increases crystal defects, which could serve to trap electrons or holes and then restrain their recombination in the film [34].

These results are confirmed by photoelectrochemical measurements, because the photocurrent is linked to the efficient generation, separation and transportation of photogenerated electron/hole pairs during light irradiation. As it can be seen in figure 6, all ZnO-coated electrodes exhibit fast and reversible photoresponses with a good reproducibility over many cycles. It is important to note that the growth mechanism of nanostructures is not affected by the nature of the substrate: morphologies, structures and compositions of nanostructures are similar on FTO substrates and on SLG substrates. Ultrathin ZnO nanowires and nanoribbons show the highest photocurrent (respectively 12 and 2.5 times higher than ZnO thin films and thick ZnO nanowires synthesized by thermal oxidation), which confirms the reduction of charge carrier recombination.

However, electron-hole pairs are generated when semiconductors are irradiated by photons with energy equal to or greater than its bandgap. In order to evaluate the bandgap of ZnO nanostructures with copper in the sub-layer, the absorption spectrum of ZnO nanowire sample is investigated through UV-visible spectrometry (figure 7). Absorbance corresponding to SLG substrate is systematically subtracted. A strong absorption peak is observed in the UV region with an absorption edge at about 375 nm (~ 3.3 eV). The optical bandgap energy (E_g)

can be calculated from the Tauc's formula, which is for direct allowed transition [35]: $(\alpha h\nu)^2 = A(h\nu - E_g)^2$, where h is Planck's constant, ν is the photon frequency, α is the absorption coefficient and A is a constant, respectively. The inset of figure 7 shows the Tauc's plot for ZnO nanowires. The optical bandgap is determined by the interception between the tangent to the linear portion of the curve and the horizontal axis. The results indicate a slight decrease in the optical bandgap value (~ 3.03 eV) by comparison with the accepted literature value of 3.27 eV for ZnO thin films [35]. Similar optical bandgap values are obtained for ZnO nanoribbons and ZnO nanocombs (2.98 eV and 3.06 eV, respectively). While the accuracy of this technique may be debatable, it seems to mean that ZnO nanostructures can mainly be activated under UV light to generate electrons and holes for the MO photodegradation, even in presence of copper in the sub-layer.

To understand the mechanism of dye degradation, different scavengers are used to investigate the main active species during the photocatalytic degradation of MO over ultrathin ZnO nanowire coated electrode (figure 8). p-benzoquinone (BQ, $O_2^{\cdot-}$ radical scavenger, 0.1mM), ammonium oxalate monohydrate (AO, hole scavenger, 10mM), dimethyl sulfoxide (DMSO, electron scavenger, 10mM) and tert-butanol (t-BuOH, $\cdot OH$ radical scavenger, 10mM) are separately added into the MO solution. The trapping experiments are carried out under light irradiation using the same experimental conditions. The degradation efficiencies decrease from 92% without scavengers to 77%, 74%, 55% and 25% in the presence of DMSO, AO, t-BuOH and BQ, respectively, which is consistent with the results of Chen et al [36] and Huang et al [37]. Thus, the superoxide $O_2^{\cdot-}$ radical is the main reactive species involved in the photocatalytic degradation of MO with ultrathin ZnO nanowire coated electrode under light irradiation.

Photocatalytic stability is another important limitation in the development of photocatalysts for organic dye degradation, mainly due to photocorrosion in the case of ZnO [4, 38]. In order to estimate the photostability of ultrathin ZnO nanowires, MO degradation is observed in repeated runs in similar experimental conditions. Five photodegradation cycles of MO solution are conducted (figure 9), which reveal only a small reduction in MO degradation after each cycle (mean value of 2.7%). Nanostructured ZnO sample continues to show considerable photocatalytic activity even after five cycles. Therefore, ZnO nanowires exhibit

good stability during the photocatalytic test, possibilities of reusability and thus could be a potential candidate for practical applications.

4. Conclusion

Ultrathin zinc oxide nanostructures have been successfully synthesized by oxidizing Cu/Zn stacks for 1 min in a flowing microwave plasma. The surface morphology can be tuned by adjusting the working pressure during oxidation process in a reproducible manner: nanowires at 200 Pa, nanoribbons at 1000 Pa and nanocombs at 2000 Pa, other experimental parameters being constant. The rapid growth of ultrathin morphologies is attributed to the afterglow area which is a very oxidizing medium since it contains high concentrations of oxygen atoms and excited oxygen molecules like $O_2(a^1\Delta_g)$, $O_2(X^3\Sigma_g^-)$ and to a lesser extent, $O_2(b^1\Sigma_g^+)$. All the produced nanostructures are single-crystalline and exhibit the wurtzite structure of ZnO. Photocatalytic activity of ZnO nanostructures is investigated from MO decomposition under light irradiation. ZnO nanowires and nanoribbons show higher photocatalytic activity compared with pure ZnO thin films without nanostructures and thick ZnO nanowires synthesized by thermal oxidation. The enhancement in photocatalytic performance could be attributed to high surface area. Moreover, these nano-objects provide at least one extremely low dimension (<10 nm). As a consequence, charge carriers need to diffuse only over a short distance to reach active sites on the surface and then can react with water molecules before their recombination. However, the results indicate that the photoinduced electrons and holes are generated almost exclusively under UV light irradiation. The possibility of reusability of ZnO nanowire samples is confirmed by a high photocatalytic activity even after several cycles of photodegradation. Thus, ultrathin ZnO nanostructures, synthesized by microwave plasma afterglow oxidation process could be considered as promising candidates to degrade organic pollutants in water.

Acknowledgments

The authors wish to thank the 'Réseau des Plasmas Froids' of CNRS/MI (France) for providing the microwave interferometer (Miwitron MWI 2650).

References

- [1] Ibhaddon A O and Fitzpatrick P 2013 Heterogeneous photocatalysis: recent advances and applications *Catalysts* 3 189–218
- [2] Hisatomi T, Kubota J and Domen K 2014 Recent advances in semiconductors for photocatalytic and photoelectrochemical water splitting *Chem. Soc. Rev.* 43 7520–35
- [3] Kumar S G and Rao K S R K 2015 Zinc oxide based photocatalysis: tailoring surface-bulk structure and related interfacial charge carrier dynamics for better environmental applications *RSC Adv.* 5 3306–51
- [4] Lee K M, Lai C W, Ngai K S and Juan J C 2016 Recent developments of zinc oxide based photocatalyst in water treatment technology: a review *Water Res.* 88 428–48
- [5] Ahmed F, Arshi N, Anwar M S, Danish R and Koo B H 2014 Morphological evolution of ZnO nanostructures and their aspect ratio-induced enhancement in photocatalytic properties *RSC Adv.* 4 29249–63
- [6] Habba Y G, Capochichi-Gnambodoe M, Serairi L and Leprince-Wang Y 2016 Enhanced photocatalytic activity of ZnO nanostructure for water purification *Phys. Status Solidi B* 253 1480–4
- [7] Han Z, Liao L, Wu Y, Pan H, Shen S and Chen J 2012 Synthesis and photocatalytic application of oriented hierarchical ZnO flower-rod architectures *J. Hazard. Mater.* 217–218 100–6
- [8] Iwu K O, Strano V, Di Mauro A, Impellizzeri G and Mirabella S 2015 Enhanced quality, growth kinetics, and photocatalysis of ZnO nanowalls prepared by chemical bath deposition *Cryst. Growth Des.* 15 4206–12
- [9] Kansal S K, Singh M and Sud D 2007 Studies on photodegradation of two commercial dyes in aqueous phase using different photocatalysts *J. Hazard. Mater.* 141 581–90
- [10] Lu F, Cai W and Zhang Y 2008 ZnO hierarchical micro/ nanoarchitectures: solvothermal synthesis and structurally enhanced photocatalytic performance *Adv. Funct. Mater.* 18 1047–56
- [11] Chang Y C 2014 Low temperature growth of ZnO nanowire arrays with enhanced high performance photocatalytic activity and reusability *Catal. Commun.* 56 45–9

- [12] Zhang Y, Ram M K, Stefanakos E K and Goswami D Y 2012 Synthesis, characterization, and applications of ZnO nanowires *J. Nanomater.* 2012 624520
- [13] Wan Q, Wang T H and Zhao J C 2005 Enhanced photocatalytic activity of ZnO nanotetrapods *Appl. Phys. Lett.* 87 083105
- [14] Murphy C J and Jana N R 2002 Controlling the aspect ratio of inorganic nanorods and nanowires *Adv. Mater.* 14 80–2
- [15] Fang Y, Pang Q, Wen X, Wang J and Yang S 2006 Synthesis of ultrathin ZnO nanofibers aligned on a zinc substrate *Small* 2 612–5
- [16] Gokarna A, Parize R, Kadiri H, Nomenyo K, Patriarche G, Miska P and Lerondel G 2014 Highly crystalline urchin-like structures made of ultra-thin zinc oxide nanowires *RSC Adv.* 4 47234–9
- [17] Gu Y, Kuskovsky L, Yin M, O'Brien S and Neumark G F 2004 Quantum confinement in ZnO nanorods *Appl. Phys. Lett.* 85 3833–5
- [18] Ghoshal T, Biswas S, Kar S, Dev A, Chakrabarti S and Chaudhuri S 2008 Direct synthesis of ZnO nanowire arrays on Zn foil by a simple thermal evaporation process *Nanotechnol.* 19 065606
- [19] Zhao C X, Li Y F, Zhou J, Li L Y, Deng S Z, Xu N S and Chen J 2013 Large-scale synthesis of bicrystalline ZnO nanowire arrays by thermal oxidation of zinc film: growth mechanism and high-performance field emission *Cryst. Growth Des.* 13 2897–905
- [20] Altaweel A, Filipic G, Gries T and Belmonte T 2014 Controlled growth of copper oxide nanostructures by atmospheric pressure micro-afterglow *J. Cryst. Growth* 407 17–24
- [21] Imam A, Boileau A, Gries T, Ghanbaja J, Mangin D, Hussein K, Sezen H, Amati M and Belmonte T 2016 Nanostructures design by plasma afterglow-assisted oxidation of iron-copper thin films *J. Cryst. Growth* 442 52–61
- [22] Kuete Saa D, Gries T, Migot-Choux S, Ghanbaja J, Boulet P, Laminsi S and Belmonte T 2017 Synthesis of RuO₂ nanowires by alkali-assisted oxidation of ruthenium in plasma afterglow at atmospheric pressure *IEEE Trans. Nanotechnol.* 16 624–33

- [23] Altaweel A, Imam A, Ghanbaja J, Mangin D, Miska P, Gries T and Belmonte T 2017 Fast synthesis of ultrathin ZnO nanowires by oxidation of Cu/Zn stacks in lowpressure afterglow Nanotechnol. 28 085602
- [24] Grotjohn T A, Asmussen J, Sivagnaname J, Story D, Vikharev A L, Gorbachev A and Kolysko A 2000 Electron density in moderate pressure diamond deposition discharges Diamond Relat. Mat. 9 322–7
- [25] Derkaoui N, Rond C, Gries T, Henrion G and Gicquel A 2014 Determining electron temperature and electron density in moderate pressure H₂/CH₄ microwave plasma J. Phys. D: Appl. Phys. 47 205201
- [26] Moisan M and Nowakowska H 2018 Contribution of surfacewave (SW) sustained plasma columns to the modeling of RF and microwave discharge with new insight into some of their features. A survey of other type of SW discharges Plasma Sources Sci. Technol. 27 073001
- [27] Touzeau M, Vialle M, Zellagui A, Gousset G, Lefebvre M and Pealat M 1991 Spectroscopic temperature-measurements in oxygen discharges J. Phys. D: Appl. Phys. 24 41–7
- [28] Mafra M, Belmonte T, Poncin-Epaillard F, Maliska A and Cvelbar U 2009 Treatment of hexatriacontane by Ar-O₂ remote plasma: formation of active species Plasma Process. Polym. 6 S198–203
- [29] Ricard A, Moisan M and Moreau S 2001 Determination, through titration with NO, of the concentration of oxygen atoms in the flowing afterglow of Ar-O₂ and N₂-O₂ plasmas used for sterilization purposes J. Phys. D: Appl. Phys. 34 1203–12
- [30] Kutasi K, Guerra V and Sa P A 2011 Active species downstream of an Ar-O₂ surface-wave microwave discharge for biomedicine, surface treatment and nanostructuring Plasma Sources Sci. Technol. 20 035006
- [31] Vesel A, Kolar M, Recek N, Kutasi K, Stana-Kleinschek K and Mozetic M 2014 Etching of blood proteins in the early and late flowing afterglow of oxygen plasma Plasma Process. Polym. 11 12–23
- [32] Kihara K and Donnay G 1985 Anharmonic thermal vibrations in ZnO Can. Mineral. 23 647–

- [33] Ren S, Bai Y F, Chen J, Deng S Z, Xu N S, Wu Q B and Yang S 2007 Catalyst-free synthesis of ZnO nanowire arrays on zinc substrate by low temperature thermal oxidation *Mater. Lett.* 61 666–70
- [34] Xu F, Shen Y, Sun L, Zeng H and Lu Y 2011 Enhanced photocatalytic activity of hierarchical ZnO nanoplate nanowire architecture as environmentally safe and facilely recyclable photocatalyst *Nanoscale* 3 5020–5
- [35] Viezbicke B D, Patel S, Davis B E and Birnie D P 2015 Evaluation of the Tauc method for optical absorption edge determination: ZnO thin films as a model system *Phys. Status Solidi B* 252 1700–10
- [36] Chen X, Wu Z, Liu D and Gao Z 2017 Preparation of ZnO photocatalyst for the efficient and rapid photocatalytic degradation of azo dyes *Nanoscale Res. Lett.* 12 143
- [37] Huang N, Shu J, Wang Z, Chen M, Ren C and Zhang W 2015 One-step pyrolytic synthesis of ZnO nanorods with enhanced photocatalytic activity and high photostability under visible light and UV light irradiation *J. Alloy. Compd.* 648 919–29
- [38] Cao Y Q, Chen J, Zhou H, Zhu L, Li X, Cao Z Y, Wu D and Li A D 2015 Photocatalytic activity and photocorrosion of atomic layer deposited ZnO ultrathin films for the degradation of methylene blue *Nanotechnol.* 26 024002

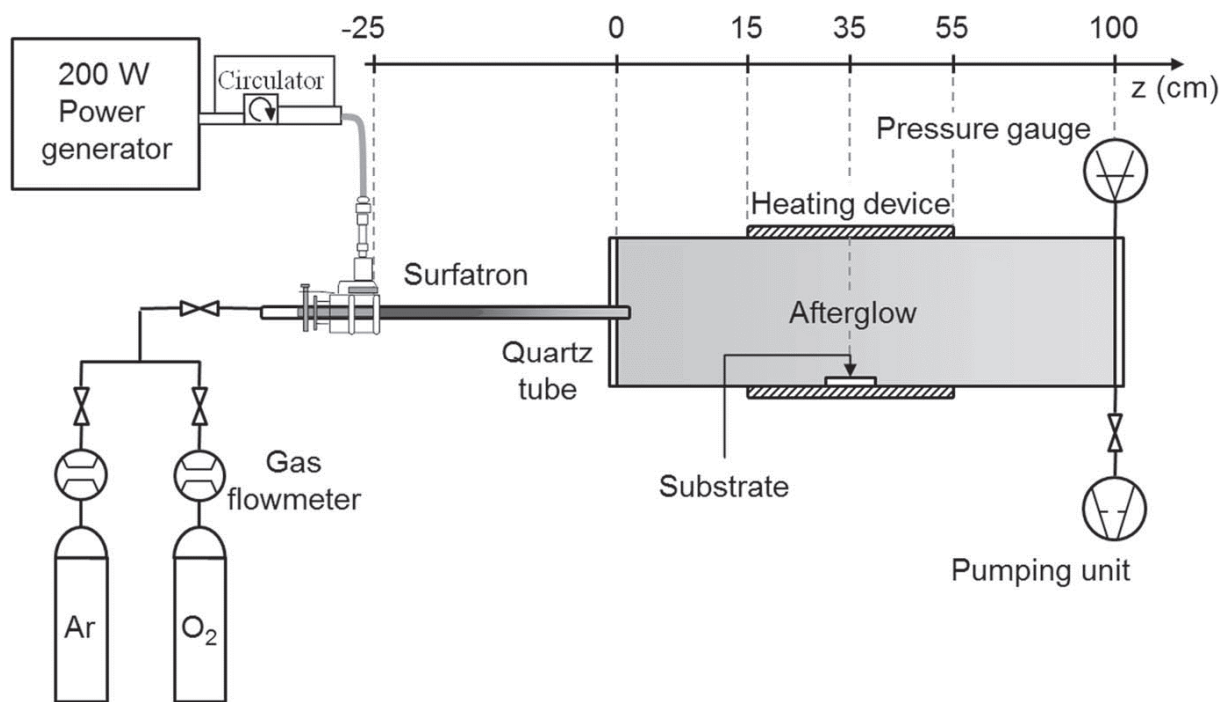


Figure 1: Experimental set-up of the flowing afterglow oxidation process.

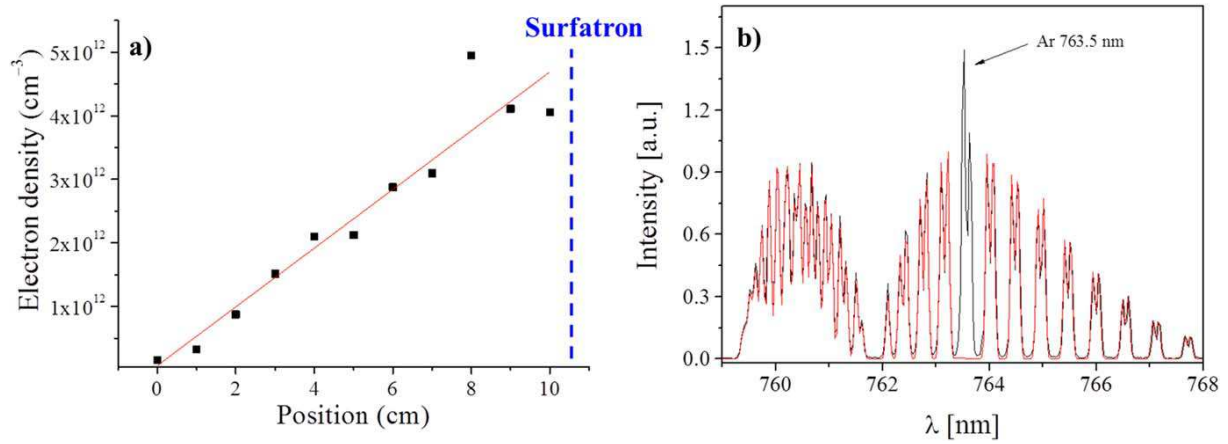


Figure 2: (a) Evolution of electron density in the plasma column as a function of the distance from the Surfatron determined by microwave interferometry. (b) Experimental (black) and simulated (red) rotational spectrum of the atmospheric band of molecular oxygen O₂ ($b^1\Sigma_g^+ \rightarrow X^3\Sigma_g^-$) recorded in the afterglow at a distance of 40 cm from the Surfatron. (560 sccm, Ar-2 vol% O₂, 200 Pa).

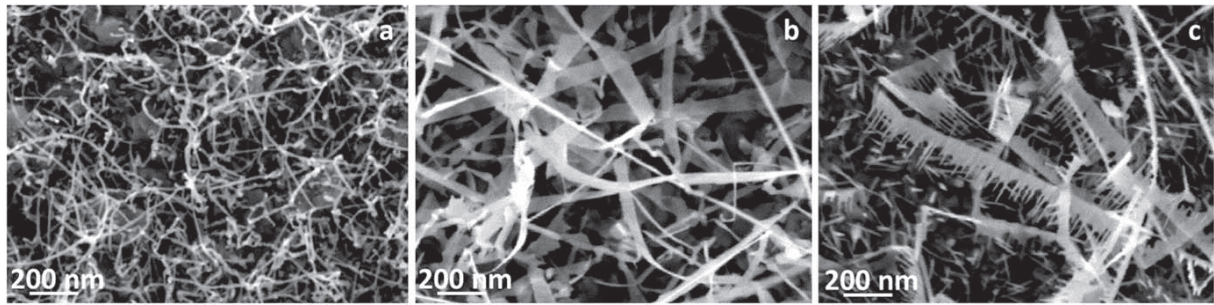


Figure 3: SEM micrographs of ZnO nanostructures synthesized in flowing microwave afterglow oxidation process as a function of working pressure: (a) nanowires at 200 Pa, (b) nanoribbons at 1000 Pa and (c) nanocombs at 2000 Pa. (Afterglow oxidation duration = 1 min).

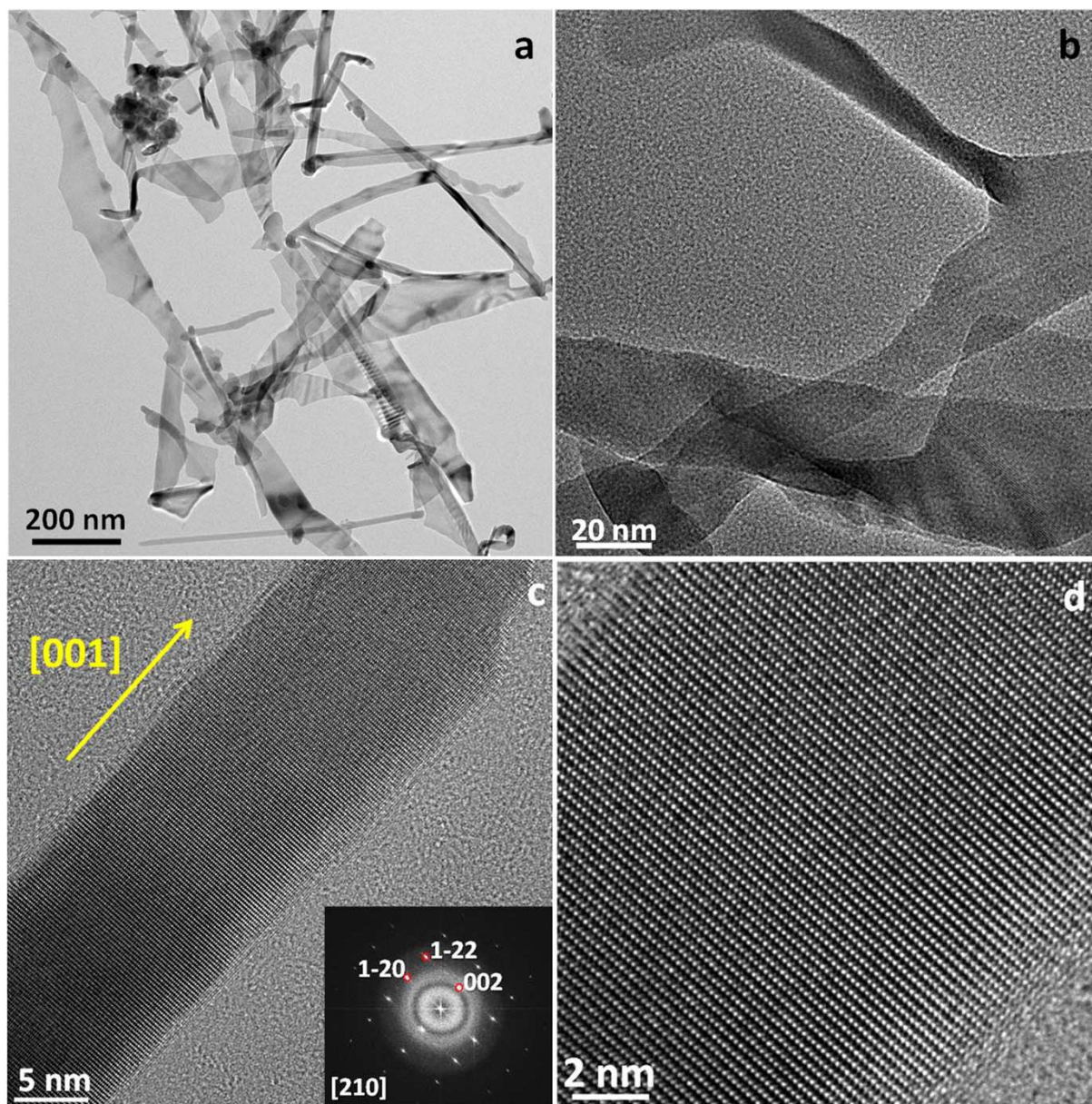


Figure 4: (a), (b) General views of nanoribbons by TEM. (c), (d) HRTEM micrographs of an individual nanoribbon at different magnifications and the corresponding FFT pattern indexed by ZnO wurtzite structure.

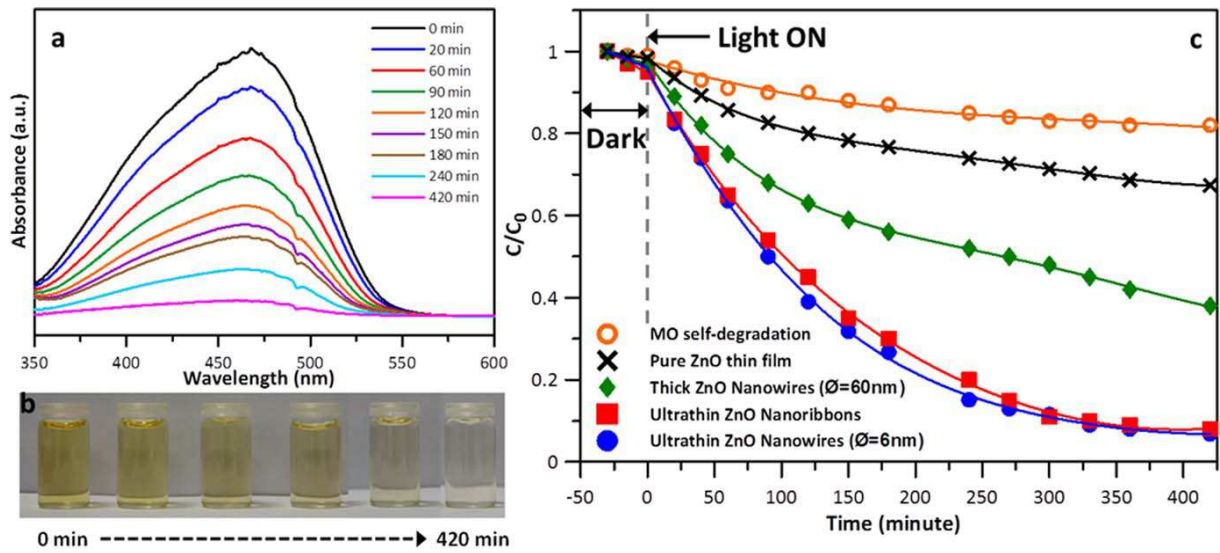


Figure 5: (a) Absorption spectra showing temporal evolution of MO degradation upon light irradiation in the presence of ZnO nanowires as photocatalyst and (b) corresponding pictures of MO solution at different exposure durations. (c) MO degradation rate without photocatalyst and with pure ZnO thin film, thick ZnO nanowires ($\phi \sim 60$ nm), ultrathin ZnO nanowires ($\phi \sim 6$ nm) and ultrathin ZnO nanoribbons, respectively.

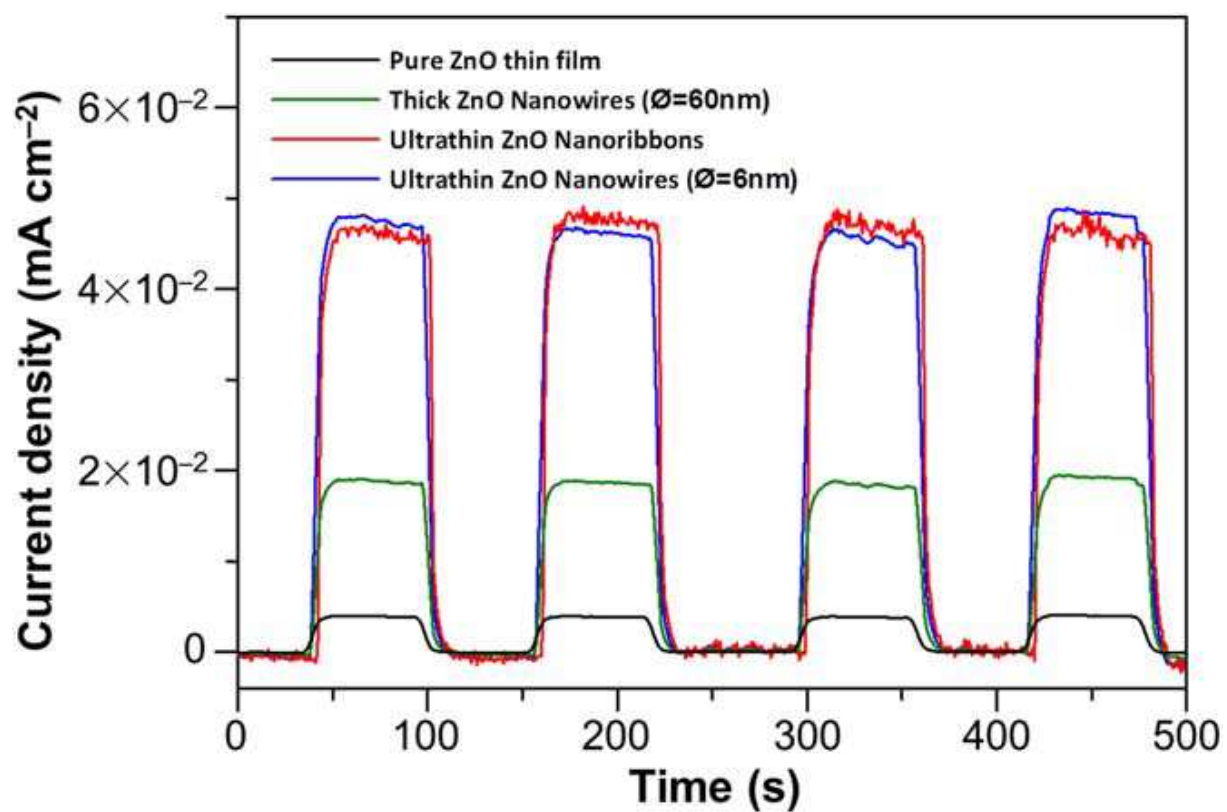


Figure 6: Transient photocurrent density responses of ZnO photocatalyst electrodes under light on-off cycles.

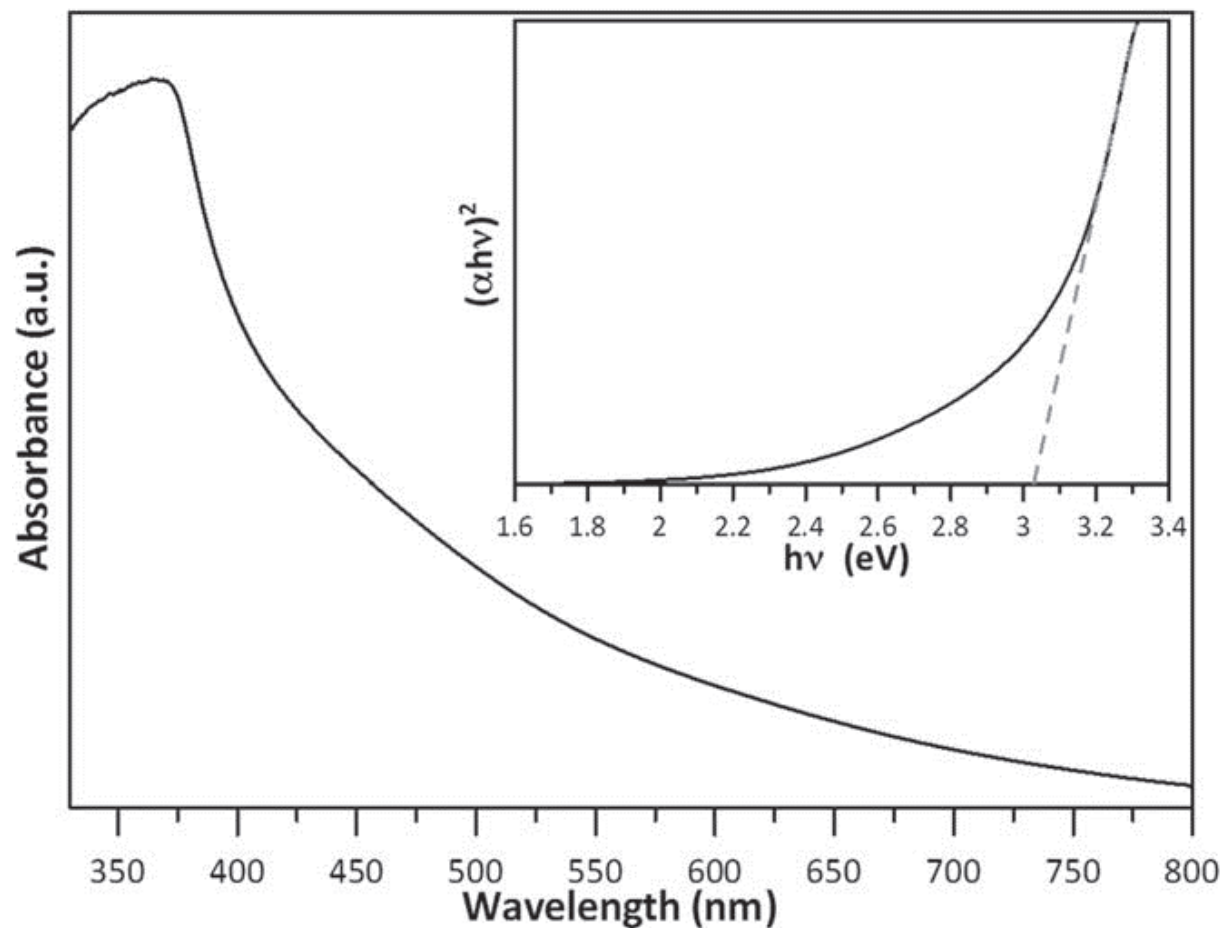


Figure 7. UV-vis absorption spectrum of ultrathin ZnO nanowires sample. The inset shows the corresponding plot of $(\alpha h\nu)^2$ versus $h\nu$.

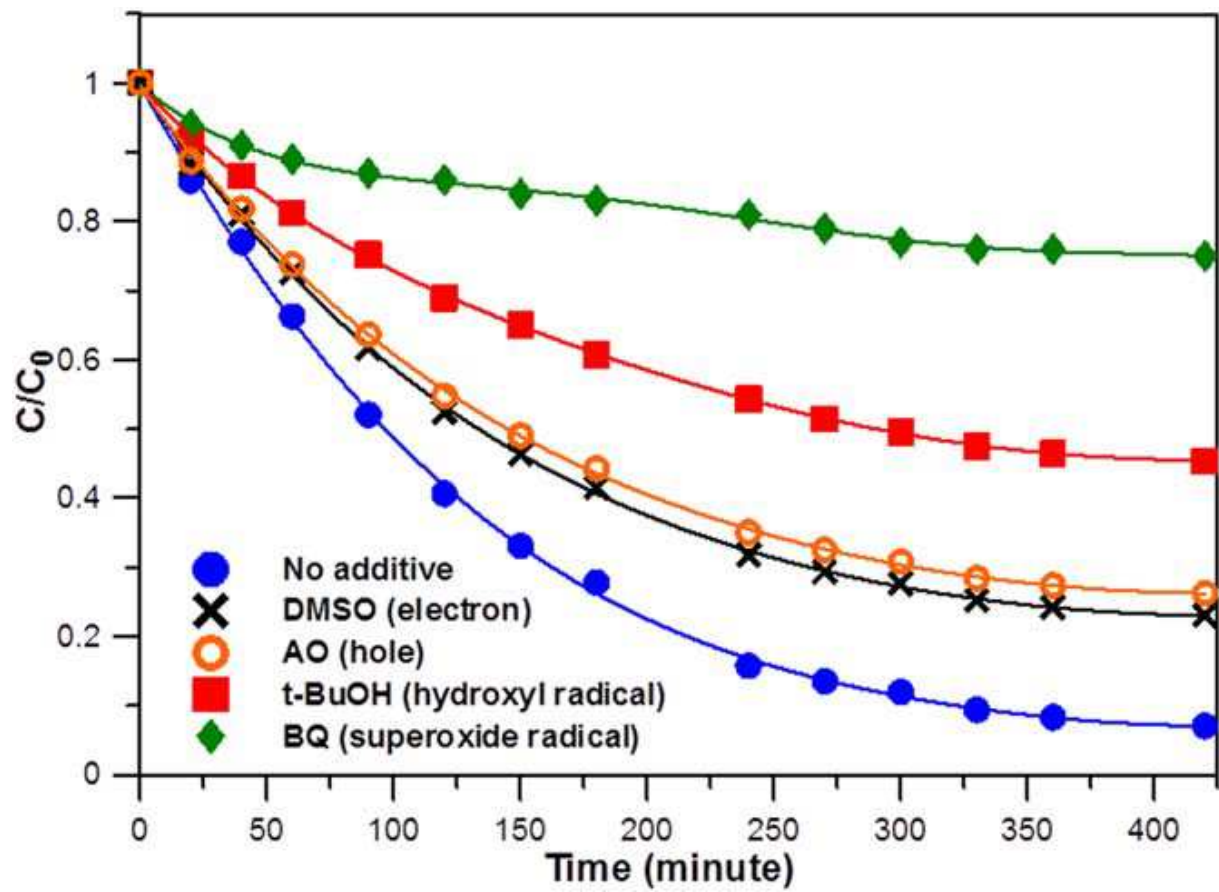


Figure 8: Influence of scavengers on the photodegradation of MO in the presence of ultrathin ZnO nanowire coated electrode under light irradiation.

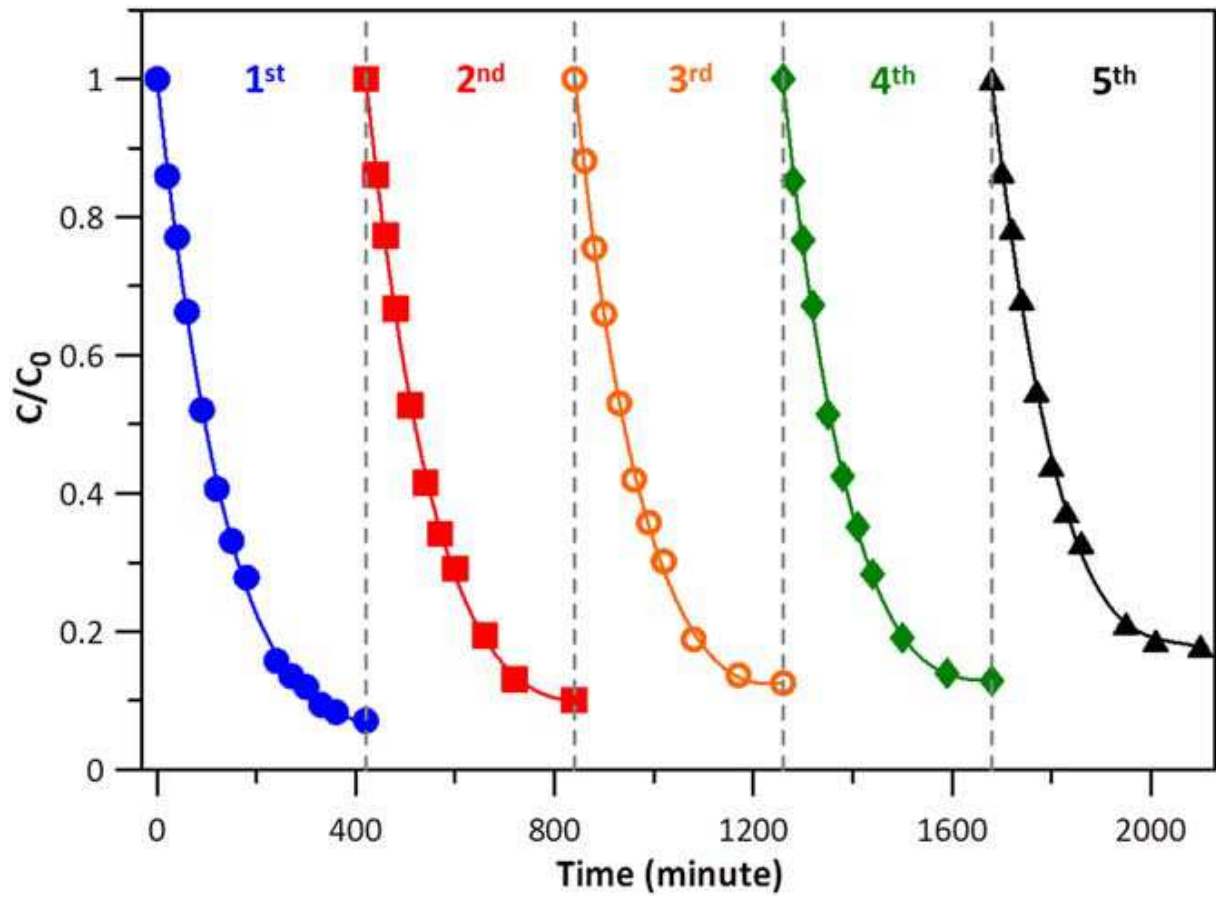


Figure 9: Recycling test in photocatalytic degradation of MO dye in water over ultrathin ZnO nanowires under light irradiation.